nature materials

Article

https://doi.org/10.1038/s41563-023-01562-9

Strongly enhanced light–matter coupling of monolayer WS_2 from a bound state in the continuum

Received: 25 September 2022

Accepted: 21 April 2023

Published online: 22 May 2023

Check for updates

Eugenio Maggiolini[1,2,6], Laura Polimeno[1,6], Francesco Todisco[1], Anna Di Renzo[1,3], Bo Han[4], Milena De Giorgi[1], Vincenzo Ardizzone[1], Christian Schneider[4], Rosanna Mastria[1], Alessandro Cannavale[1,5], Marco Pugliese[1], Luisa De Marco[1], Aurora Rizzo[1], Vincenzo Maiorano[1], Giuseppe Gigli[1,3], Dario Gerace[2], Daniele Sanvitto[1] ✉ & Dario Ballarini[1] ✉

Exciton–polaritons derived from the strong light–matter interaction of an optical bound state in the continuum with an excitonic resonance can inherit an ultralong radiative lifetime and significant nonlinearities, but their realization in two-dimensional semiconductors remains challenging at room temperature. Here we show strong light–matter interaction enhancement and large exciton–polariton nonlinearities at room temperature by coupling monolayer tungsten disulfide excitons to a topologically protected bound state in the continuum moulded by a one-dimensional photonic crystal, and optimizing for the electric-field strength at the monolayer position through Bloch surface wave confinement. By a structured optimization approach, the coupling with the active material is maximized here in a fully open architecture, allowing to achieve a 100 meV photonic bandgap with the bound state in the continuum in a local energy minimum and a Rabi splitting of 70 meV, which results in very high cooperativity. Our architecture paves the way to a class of polariton devices based on topologically protected and highly interacting bound states in the continuum.

Bound states in the continuum (BICs) are solutions of a wave equation that lie within the range of continuum energy states, but without any coupling to far-field radiation[1,2]. As a consequence, BICs are characterized by extremely large quality (Q) factors, only limited by material losses. Moreover, in some cases, they can feature topological protection, resulting in high robustness to external perturbations and fabrication imperfections[3]. Despite being conceived as potential engineering tools to confine electrons—and as such, difficult to realize—they have recently been extended to many wave phenomena in periodic lattices, spanning from the acoustic[4–6] to the electromagnetic[7,8] domain.

Owing to the advances in materials processing, nanophotonics has rapidly emerged as a fruitful platform to develop structures sustaining optical BICs, which have been observed in several architectures including photonic crystals[8] (PhCs), waveguides[9] and metasurfaces[10]. The large Q factor of these states makes nanophotonic BICs extremely appealing for enhancing light–matter interactions when integrated with optically active materials[11,12]. From this point of view, strongly

[1]CNR NANOTEC, Institute of Nanotechnology, Lecce, Italy. [2]Dipartimento di Fisica, Università di Pavia, Pavia, Italy. [3]Dipartimento di Matematica e Fisica E. De Giorgi, Università del Salento, Lecce, Italy. [4]Institute of Physics, University of Oldenburg, Oldenburg, Germany. [5]Department of Civil Engineering Sciences and Architecture, Polytechnic University of Bari, Bari, Italy. [6]These authors contributed equally: E. Maggiolini, L. Polimeno.
✉e-mail: daniele.sanvitto@nanotec.cnr.it; dario.ballarini@nanotec.cnr.it

coupled BICs with different materials have been reported[13,14], giving rise to unique optical properties of the so-called exciton–polaritons. These bosonic quasi-particles, arising from the strong coupling between excitons and photons[15], acquire hybrid properties inherited from their bare components, among which the strongly interacting character is one of the most pursued.

Exciton–polariton BICs show increased lifetimes compared with standard exciton–polaritons[13,14]. This is a crucial step to bring polariton physics to robust room-temperature operation, paving the way for the realization of ultrafast nonlinear electro-optical applications, such as low-threshold lasing[16], information processing and logic operations[17]. The first milestone in this direction has been recently achieved with the demonstration of polariton condensation from a BIC by using patterned GaAs waveguides at cryogenic temperatures[18]. With the aim of achieving room-temperature nonlinear operation, exciton–polaritons in semiconductors with larger exciton binding energy are required. In this respect, atomically thin transition metal dichalcogenides (TMDs) represent an ideal active medium for realizing room-temperature polariton systems, owing to a stable excitonic resonance arising from their two-dimensional confinement and reduced dielectric screening[19–21]. However, coupling photonic BICs with single monolayers poses further issues, since transverse-electric modes are strongly confined within waveguides, whereas the two-dimensional semiconductor can only be deposited at their surface, rendering the exciton–photon coupling fairly weak. In the few experimental realizations so far, a TMD monolayer is transferred on top of the patterned PhC slab, limiting the overlap between the electric-field profile and the exciton wavefunction, thereby resulting in a vacuum Rabi splitting comparable with the exciton linewidth[22].

An alternative solution is provided by Bloch surface waves (BSWs), evanescent electromagnetic modes propagating at the interface between a distributed Bragg reflector (DBR) and the surrounding medium[23]. In a BSW, the electric-field enhancement is localized at the surface of the dielectric substrate, allowing narrow resonances that strongly couple with thin films deposited on top of the DBR, such as organic materials[24] or TMDs[25]. Moreover, in the context of our BIC design, BSWs allow for a flexible and sensitive tuning of their spatial field profiles, owing to their ability to effectively support modes in both gaps and fills of the pattern and with superior implementability from the fabrication point of view[26].

In this work, we report the systematic engineering and observation of a topologically protected BIC in an energy minimum of a BSW polariton dispersion. We achieve a large strong coupling of 70 meV between the photonic BIC and a tungsten disulfide (WS_2) monolayer, demonstrating strong polariton nonlinearities at room temperature. These results follow from original photonic engineering and algorithmic optimization of the surface pattern, which allows to simultaneously fulfil several stringent requirements: (1) maximizing the light–matter interaction between a photonic BIC branch and the TMD neutral exciton; (2) minimizing the light–matter interaction between the lossy mode (lower Bloch mode) and the TMD neutral exciton; (3) BIC polariton deterministically placed at the local minimum of the energy dispersion, rather than the maximum as commonly realized; (4) large energy gap between the BIC branch and lower (lossy) branch; (5) dispersion shape and tuning tolerant to fabrication imperfections.

Device architecture and energy–momentum dispersions

Our sample architecture is sketched in Fig. 1a and consists of a layered SiO_2–TiO_2 DBR, on top of which we place a non-trivial one-dimensional PhC, finely optimized by an algorithmic approach (Supplementary Sections A–C). The DBR structure has a stop band centred at 1,476 meV, supporting a transverse-electric BSW beyond the light cone, with energy $E_{BSW} \simeq 2$ eV at $k = 11.3\ \mu m^{-1}$ (Supplementary Fig. 1A). A WS_2 monolayer is placed on top of the DBR using a dry transfer method and then covered with a 20-nm-thick SiO_2 layer by an electron-beam evaporation process (Methods). The capped WS_2 monolayer supports a sharp excitonic resonance at 2,024 meV (Supplementary Fig. 2), crossing the BSW dispersion beyond the light cone. We measure the reflection spectrum of the coupled WS_2-BSW system in the in-plane momentum space by using an oil-immersion objective, showing the typical anticrossing behaviour of the strong-coupling regime (Supplementary Fig. 1B). The grating is fabricated on top of the SiO_2 capping layer by low-dose and low-stress electron-beam lithography of a polymethyl methacrylate (PMMA) thin film (Methods). Owing to multiple harmonics in the Fourier spectrum and the numerical optimization of the geometric parameters, the grating is able to fold the BSW polariton dispersion and to enforce a BIC at zero momentum with maximum light–matter interaction. The reflectivity spectrum of the fabricated device, measured in the Fourier space in the region around $k = 0$, is shown in Fig. 1b and compared with a simulated dispersion from rigorous coupled-wave analysis in Fig. 1c (Supplementary Fig. 1C provides details on the graphics).

Design and optimization approach

Among the possible optical BICs one can mould through a PhC patterning, here we focus on the specific case of the topologically protected BICs occurring at the Γ points in the reciprocal lattice of a one-dimensional PhC. These BICs—among the first to be studied in photonics[2]—are antisymmetric modes with respect to the real-space symmetry axes of the lattice; as such, they cannot couple to the continuum of radiation in free space, which is symmetric at the Γ point. In the limited number of other BIC polariton realizations in the literature[22,27], symmetry breaking in the PhC pattern leads to quasi-BICs instead of topological BICs. Here we adopt a different approach to simultaneously deliver all the requirements mentioned in the introduction. As we thoroughly show in Supplementary Section B and Supplementary Fig. 3, by an alternate deformation or a periodic removal of posts from a simple one-dimensional grating, we are able to artificially build a Fourier spectrum in reciprocal space with a large subwavelength component, which ensures a large energy gap, whereas tunable super-wavelength components ensure to replicate the dispersion at zero momentum, where it can be optically pumped and observed with ease. The specific solution of the periodic post removal, implemented in the device fabricated and measured here, allows to build a Fourier spectrum fundamentally robust to nanofabrication inaccuracies. Furthermore, as we show in Supplementary Fig. 4, our original design breaks the simple periodic structure of a regular grating and allows to deterministically associate the axes of symmetry of the periodic cell to the material with a higher refractive index (PMMA) or smaller refractive index (air); this is done by simultaneously preserving the full point-group symmetry of the original cell. As a consequence, the BIC results deterministically pinned in the upper or lower Bloch mode, as a function only of the parity of the number of pillars within each unit cell, simultaneously preserving its topological nature. As a second consequence, the filling factor parameter, which in a regular grating is necessary for the tuning of the BIC to be in the upper or lower photonic branch, is now made entirely unnecessary for such tuning and can be fully leveraged for the purpose of optimizing the bandgap and light–matter interaction.

Nevertheless, a crucial point of our approach, allowing to meet requirements (1) and (2) discussed earlier, resides in the simultaneous co-engineering of all the geometric parameters of the structure by a design strategy that combines original heuristic considerations (Supplementary Section B) and a globally converging algorithm (Supplementary Section C). Namely, we combine heuristic physical considerations in setting finite-difference time-domain simulations and in devising a figure of merit to be optimized, with a particle swarm optimization algorithm. The reasons for a structured numerical optimization are related to the non-perturbative character that a surface patterning introduces to the BSW mode, which on one hand prevents to effectively tune the system by acting on single geometric parameters and, on the other hand, is a powerful lever to meet demanding objectives,

https://doi.org/10.1038/s41563-023-01562-9

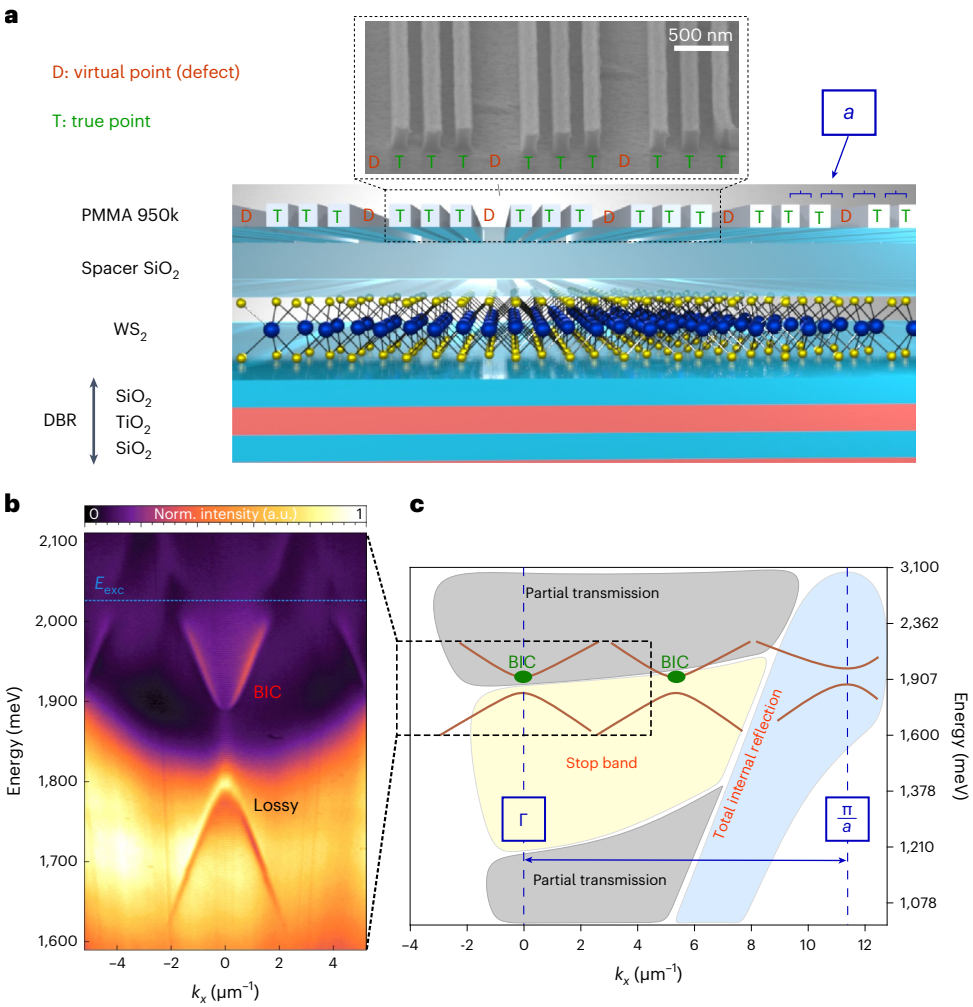

Fig. 1 | Overall device architecture and energy–momentum dispersions. **a**, Sketch of the device. The PMMA grating is fabricated on the top of a DBR–WS_2–SiO_2 structure with a defected subwavelength structure; the ridges marked by D are systematically missing, leading to harmonics at $K_G/4$, $K_G/2$, $3K_G/4$ and K_G (Supplementary Section A), where $K_G = \frac{\pi}{a}$ and a is the subwavelength periodicity. The inset shows the scanning electron microscopy image illustrating the high-aspect-ratio fabrication process, where each three-element grating unit is made up of two lateral ridges of ~177 nm width and a central ridge of ~118 nm width. **b**, Experimental reflectivity in momentum space of the sample, with a zoomed-in view of the region close to $k \approx 0$. **c**, Rigorous coupled-wave analysis simulation of the grating effect on the BSW supported by the DBR. The defected grating harmonic K_G induces a wide gap opening at the band edge, whereas the $K_G/2$ harmonic mirrors the dispersion to $k \approx 0$, leading to a BIC at the Γ point.

such as a strong enhancement of the light–matter interaction in a given mode (in our case, the upper Bloch branch hosting the BIC) and strongly quenching such interaction for another mode (the lossy Bloch branch). Finally, our numerical approach is robust in optimizing the light–matter interaction from the weak to the strong-coupling regime (Supplementary Section D).

Strong coupling and room-temperature nonlinearities

The energy versus in-plane momentum photoluminescence (PL) of the WS_2 monolayer after the fabrication of the grating is shown in Fig. 2a, off-resonantly excited by a continuous-wave 488 nm diode laser. The formation of BIC polaritons in the minimum of the energy dispersion at $k = 0$ is clearly visible as a vanishing intensity for $k \to 0$, where destructive interference in the far-field radiation induces light trapping in the near field. The experimental Q values (red square) and polariton linewidths (black dots) in the BIC branch are reported as a function of the in-plane momentum (Fig. 2b). Decreasing the in-plane momentum, the polariton linewidth narrows and results in a burst of Q factor when approaching $k = 0$. The presented Q-factor values are extracted from a PL measurement on the 'loaded' dispersion—that is, the photonic dispersion coupled to the active material—so they are underestimations of the true photonic Q factor, since they include the non-radiative contribution from the WS_2 monolayer.

The anticrossing of the BIC branch with the monolayer exciton is shown in detail in Fig. 2c and fit with a method that is thoroughly described in Supplementary Section E and Supplementary Fig. 9. Here we extract a Rabi splitting of $\Omega_{Rabi} \approx 70$ meV, corresponding to a light–matter interaction constant $g \approx 40$ meV, which is obtained from the identity $\Omega_{Rabi} = \sqrt{4g^2 - \Delta_\gamma^2}$ and the difference Δ_γ between the measured linewidth for neutral exciton Γ_{exc} (PL measurement) and the linewidth of the unloaded photonic mode Γ_{ph} at the anticrossing (reflection measurement without a WS_2 monolayer). Our result is larger than previous values of Rabi splitting obtained for TMDs in the strong-coupling regime, both in planar dielectric microcavities[20,28–31] and in other nanophotonic structures[22,25,32]. Comparable light–matter interaction strengths have only been demonstrated in plasmonic structures, which leverage on the subwavelength confinement[33–35], but at the price of large non-radiative losses.

https://doi.org/10.1038/s41563-023-01562-9

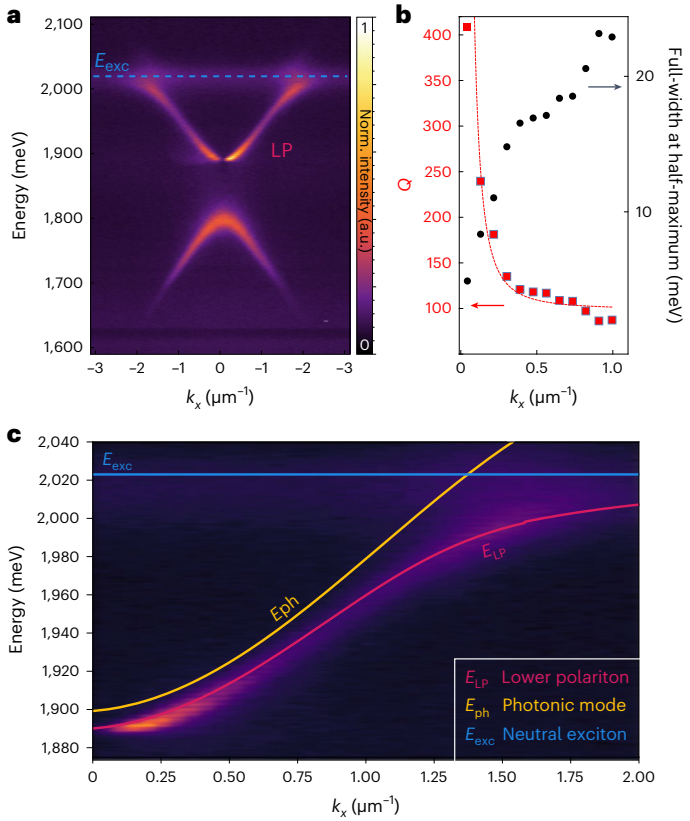

Fig. 2 | PL measurements and polariton BIC. a, Upper BIC-like mode strongly coupled with the WS_2 monolayer exciton (blue line), as observable from the anticrossing, and weakly coupled lower lossy mode. **b**, *Q*-factor values (black dots) and polariton linewidths (red squares) plotted as a function of the in-plane momentum. **c**, Fitting of the PL dispersion at the anticrossing, used to extract the Rabi splitting. The blue solid line represents the E_{exc} resonance; the yellow solid line, photonic dispersion E_{ph} extrapolated from reflection measurements on a TMD-free area; the red solid line, the fitted polaritonic dispersion for a 70 meV Rabi splitting.

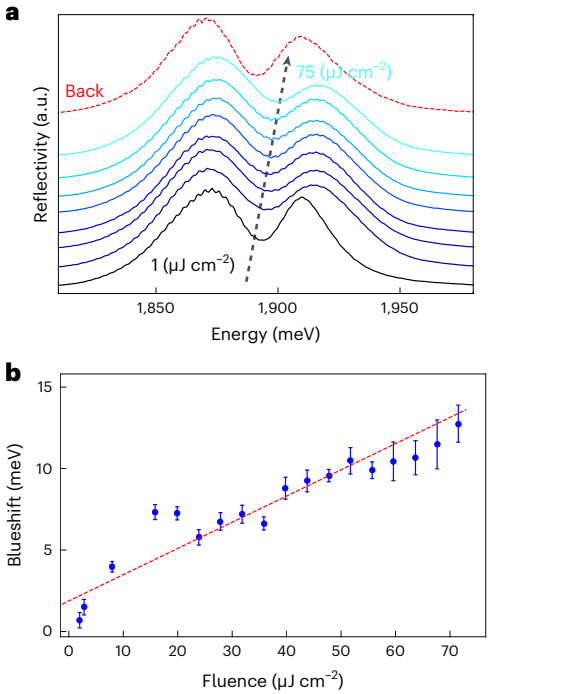

Fig. 3 | Nonlinear shift of the polariton BIC. a, Reflection spectra of the pulsed laser in the polariton mode at $k \approx 0.5$ μm^{-1}, corresponding to different resonant excitation fluences. **b**, Energy blueshift of the polariton modes at $k \approx 0.5$ μm^{-1} as a function of incident fluence. The reflection dip for each fluence is fitted with a Gaussian curve by the least-squares method. The error bar for each fluence represents the standard error on the Gaussian mean obtained from the fit.

In fact, the present platform establishes a record in terms of the key figure of merit to characterize the regime of light–matter interaction[36], which is the cooperativity $C = \frac{4g^2}{\Gamma_{exc} \times \Gamma_{ph}}$. In Supplementary Table 3, we comparatively reviewed a large number of platforms displaying the strong-coupling regime on a WS_2 monolayer at room temperature: the topologically protected BIC BSW overcomes all the full-dielectric platforms in terms of both Rabi splitting and cooperativity; it also overcomes all plasmonic or metal-based systems in terms of cooperativity alone, due to the combination of a large Rabi splitting with a narrow linewidth. At the same time, we achieve a suppression of the light–matter interaction between the TMD and lossy branch, with a fitted value $g_{lossy} \approx 21$ meV that clearly puts the lossy branch in the weak-coupling regime (Supplementary Section E, Supplementary Fig. 10 and Supplementary Table 2). The combination of suppressed g_{lossy}/g_{BIC} ratio and the large bandgap gives us a peculiar system with a highly interacting upper Bloch mode (BIC) and a weakly coupled lower Bloch mode (lossy).

The room-temperature strong coupling of the BIC branch enables a powerful platform for nonlinear applications that exploit the excitonic nonlinearity to shift the polariton resonance[17,37,38]. The nonlinear polariton behaviour originates from two contributions, namely, the Coulomb exchange interaction between excitons and the reduction in exciton–photon coupling due to the Pauli-blocking principle[39–41].

In the mean-field approximation, the overall nonlinearity induces an energy blueshift ΔE_{pol} of the polariton resonance:

$$\Delta E_{pol} = g_{pol} \times n_{pol}, \quad (1)$$

where n_{pol} is the polariton density, proportional to the excitation power, and g_{pol} is the polariton nonlinearity.

Figure 3a shows that the reflectivity spectrum of the laser (centred at ~1.9 eV) changes as the incident power is increased. Here the low-fluence spectrum (black solid line) shows that the absorption of polariton resonance shifts towards higher energies as the incident fluence increases (light-blue solid line), recovering its initial lineshape when the incident fluence is lowered again (red dashed line). This reversibility guarantees that the blueshift is not due to degradation of the material, but that it arises from polariton interactions. In the moderate range of laser fluences explored in this work, we are able to observe a blueshift of 13 meV, almost three times the full linewidth of the BIC polariton, owing to the large cooperativity. By fitting the data reported in Fig. 3a as a function of the incident fluence with a straight line (Fig. 3b), we estimate the polariton interaction constant at room temperature using equation (1): $g_{pol} \approx 5.8 \times 10^{-4}$ μeV μm^2. To extract the value of exciton interaction constant g_{exc}, we first evaluate the exciton fraction for the polariton mode, $X = |C_{Hp}|^2$, in which C_{Hp} is the excitonic Hopfield coefficient (Supplementary Section D). Considering that the detuning of the pumped mode is $\delta \approx 108$ meV and the Rabi splitting is $\Omega \approx 70$ meV, the polariton excitonic fraction of the analysed mode is $X \approx 0.08$. From this, we extract an excitonic interaction constant $g_{exc} \approx 6 \times 10^{-2}$ μeV μm^2, in agreement with the g_{exc} value found for WS_2 monolayers at room temperature[25].

The g_{exc} value extracted from this analysis neglects any loss in the material; therefore, it constitutes a lower limit for the interaction

https://doi.org/10.1038/s41563-023-01562-9

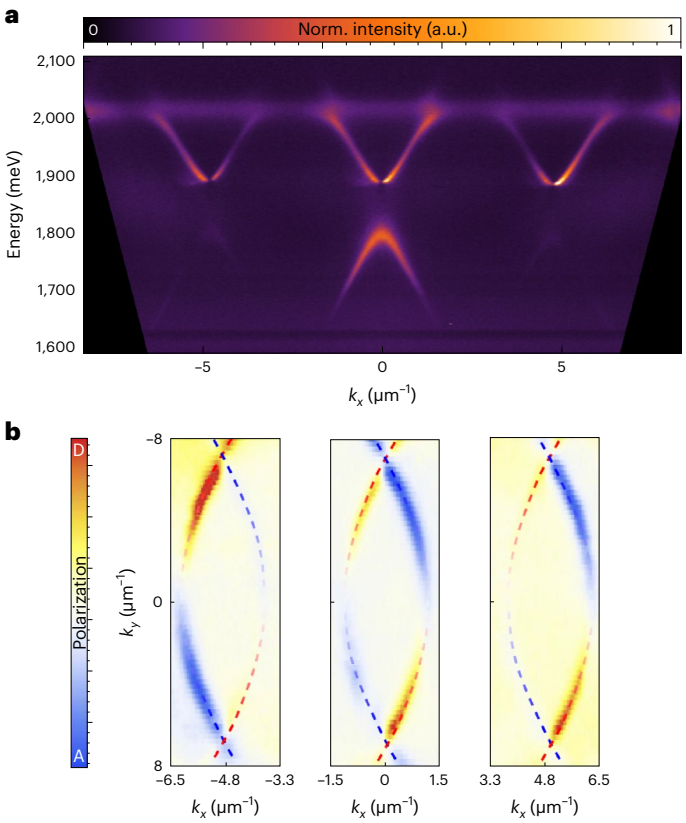

Fig. 4 | Topological nature of polariton BIC and its replicas. a, Energy versus in-plane momentum PL of WS_2 monolayer in which Γ-point replicas are clearly visible at higher in-plane wavevectors. **b**, Degree of linear polarization in diagonal basis for all BIC BSW replicas. The dashed lines are a guide for the eye to underline the rotation of linear polarization.

strength, effectively confirming that the active material is preserved after the capping and patterning process.

Topological nature of BIC BSW

In Fig. 4a, we show the PL dispersion along the k_x direction, when pumping the WS_2 monolayer off resonance (~2,540 meV). The super-wavelength components of the grating (Supplementary Section B and Supplementary Fig. 3) lead to the formation of Γ-point replicas within the light cone, with three BICs in a local minimum of the dispersion. To confirm the topological nature of the measured BIC polaritons, we directly extract the degree of linear polarization of the far-field radiation, in the diagonal–antidiagonal basis, defined as $(I_D - I_A)/(I_D + I_A)$, where I_D and I_A are the intensities of the diagonal and antidiagonal polarization components of the electric field, with respect to the $\hat{x}, \hat{y}$ natural directions of the grating pattern. In Fig. 4b, three polarization vortices are clearly visible in the k_x–k_y plane, scanning slightly above the energy of the BIC (~1,900 meV). This result shows the peculiar topological nature for both the Γ_0 BIC and its higher-order replicas. The qualitative appearance of the winding pattern consistently supports the evidence of a $|q| = 1$ topological charge, with the polarization vector rotating by 2π for a simple closed path around each BIC singularity. All these experimental evidences can be supported by analytic derivations (Supplementary Section F).

Discussion

Combining the enhanced Coulomb interactions in a WS_2 monolayer and flexible tunability of a topologically protected BIC resonance in the BSW polariton dispersion, we propose and experimentally show a robust platform to explore and leverage the rich physics of two-dimensional semiconductors in a system that is completely open to the environment. Owing to the large cooperativity, we can achieve substantial polariton nonlinearities close to a BIC at room temperature. Moreover, although BICs have been typically realized on the energy maxima (lower band) of PhC waveguide modes[12,18,22], we show that topological BICs at an energy minimum of the dispersion (upper band) can be formed and optimized for maximum light–matter interaction well beyond the present state of the art.

We are able to reach the abovementioned results having the two-dimensional material successfully encapsulated in a glass stack and the BIC polariton resonance spatially enhanced at the level of the active material as well as open air. The possibilities offered by a platform of this kind, with an active part well protected but yet able to strongly interact with the environment above, range, for instance, from applications in biomolecular sensing—through embedding in microfluidic systems—to fundamental studies on dipolar interactions[42], Rydberg polaritons[41,43] and electrically tuned non-neutral optical transitions[44] in TMDs, with the possible integration of transparent contact layers.

Online content

Any methods, additional references, Nature Portfolio reporting summaries, source data, extended data, supplementary information, acknowledgements, peer review information; details of author contributions and competing interests; and statements of data and code availability are available at https://doi.org/10.1038/s41563-023-01562-9.

References

1. von Neumann J. & Wigner, E. P. Über merkwürdige diskrete Eigenwerte. in *The Collected Works of Eugene Paul Wigner* Vol. A/1 (Springer, 1993).
2. Zhen, B., Hsu, C. W., Lu, L., Stone, A. D. & Soljačić, M. Topological nature of optical bound states in the continuum. *Phys. Rev. Lett.* **113**, 257401 (2014).
3. Jin, J. et al. Topologically enabled ultrahigh-*Q* guided resonances robust to out-of-plane scattering. *Nature* **574**, 501–504 (2019).
4. Xiao, Y. X., Ma, G., Zhang, Z. Q. & Chan, C. T. Topological subspace-induced bound state in the continuum. *Phys. Rev. Lett.* **118**, 166803 (2017).
5. Haq, O. & Shabanov, S. Bound states in the continuum in elasticity. *Wave Motion* **103**, 102718 (2021).
6. Deriy, I., Toftul, I., Petrov, M. & Bogdanov, A. Bound states in the continuum in compact acoustic resonators. *Phys. Rev. Lett.* **128**, 084301 (2022).
7. Capasso, F. et al. Observation of an electronic bound state above a potential well. *Nature* **358**, 565–567 (1992).
8. Dai, S., Hu, P. & Han, D. Near-field analysis of bound states in the continuum in photonic crystal slabs. *Opt. Express* **28**, 16288–16297 (2020).
9. Bezus, E. A., Bykov, D. A. & Doskolovich, L. L. Bound states in the continuum and high-*Q* resonances supported by a dielectric ridge on a slab waveguide. *Photon. Res.* **6**, 1084–1093 (2018).
10. Muhammad, N., Chen, Y., Qiu, C.-W. & Wang, G. P. Optical bound states in continuum in MoS_2-based metasurface for directional light emission. *Nano Lett.* **21**, 967–972 (2021).
11. Joseph, S., Pandey, S., Sarkar, S. & Joseph, J. Bound states in the continuum in resonant nanostructures: an overview of engineered materials for tailored applications. *Nanophotonics* **10**, 4175–4207 (2021).
12. Dang, N. H. M. et al. Realization of polaritonic topological charge at room temperature using polariton bound states in the continuum from perovskite metasurface. *Adv. Opt. Mater.* **10**, 2102386 (2022).

13. Koshelev, K. L., Sychev, S. K., Sadrieva, Z. F., Bogdanov, A. A. & Iorsh, I. V. Strong coupling between excitons in transition metal dichalcogenides and optical bound states in the continuum. *Phys. Rev. B* **98**, 161113(R) (2018).
14. Lu, L. et al. Engineering a light–matter strong coupling regime in perovskite-based plasmonic metasurface: quasi-bound state in the continuum and exceptional points. *Photon. Res.* **8**, A91–A100 (2020).
15. Kavokin, A., Baumberg, J., Malpuech, G. & Laussy, F. *Microcavities* (Oxford Univ. Press, 2008).
16. Kodigala, A. et al. Lasing action from photonic bound states in continuum. *Nature* **541**, 196–199 (2017).
17. Sanvitto, D. & Kéna-Cohen, S. The road towards polaritonic devices. *Nat. Mater.* **17**, 1061–1073 (2016).
18. Ardizzone, V. et al. Polariton Bose–Einstein condensate from a bound state in the continuum. *Nature* **605**, 447–454 (2022).
19. Zhao, J. et al. Ultralow threshold polariton condensate in a monolayer semiconductor microcavity at room temperature. *Nano Lett.* **21**, 3331–3339 (2021).
20. Anton-Solanas, C. et al. Bosonic condensation of exciton–polaritons in an atomically thin crystal. *Nat. Mater.* **20**, 1233–1239 (2021).
21. Manzeli, S., Ovchinnikov, D., Pasquier, D., Yazyev, O. V. & Kis, A. 2D transition metal dichalcogenides. *Nat. Rev. Mater.* **2**, 17033 (2017).
22. Kravtsov, V. et al. Nonlinear polaritons in a monolayer semiconductor coupled to optical bound states in the continuum. *Light. Sci. Appl.* **9**, 56 (2020).
23. Meade, R. D., Brommer, K. D., Rappe, A. M. & Joannopoulos, J. D. Electromagnetic Bloch waves at the surface of a photonic crystal. *Phys. Rev. B* **44**, 10961–10964 (1991).
24. Lerario, G. et al. Room temperature Bloch surface wave polaritons. *Opt. Lett.* **39**, 2068–2071 (2014).
25. Barachati, F. et al. Interacting polariton fluids in a monolayer of tungsten disulfide. *Nat. Nanotechnol.* **13**, 906–909 (2018).
26. Bezus, E. A., Bykov, D. A. & Doskolovich, L. L. Integrated diffraction gratings on the Bloch surface wave platform supporting bound states in the continuum. *Nanophotonics* **10**, 4331–4340 (2021).
27. Weber, T. et al. Strong light-matter interaction with self-hybridized bound states in the continuum in monolithic van der Waals metasurfaces. Preprint at https://arxiv.org/abs/2209.01944 (2022).
28. Ardizzone, V. et al. Emerging 2D materials for room-temperature polaritonics. *Nanophotonics* **8**, 1547–1558 (2019).
29. Xenogiannopoulou, E. et al. High-quality, large-area $MoSe_2$ and $MoSe_2/Bi_2Se_3$ heterostructures on AlN/Si substrates by molecular beam epitaxy. *Nanoscale* **7**, 7896–7905 (2015).
30. Lackner, L. et al. Tunable exciton-polaritons emerging from WS_2 monolayer excitons in a photonic lattice at room temperature. *Nat. Commun.* **12**, 4933 (2021).
31. Shan, H. et al. Spatial coherence of room-temperature monolayer WSe_2 exciton-polaritons in a trap. *Nat. Commun.* **12**, 6406 (2021).
32. Rosser, D. et al. Dispersive coupling between $MoSe_2$ and an integrated zero-dimensional nanocavity. *Opt. Mater. Express* **12**, 59–72 (2022).
33. Wang, S. et al. Coherent coupling of WS_2 monolayers with metallic photonic nanostructures at room temperature. *Nano Lett.* **16**, 4368–4374 (2016).
34. Lundt, N. et al. Observation of macroscopic valley-polarized monolayer exciton-polaritons at room temperature. *Phys. Rev. B* **96**, 241403 (2017).
35. Qin, J. et al. Revealing strong plasmon-exciton coupling between nanogap resonators and two-dimensional semiconductors at ambient conditions. *Phys. Rev. Lett.* **124**, 063902 (2020).
36. Rodriguez, S. R.-K. Classical and quantum distinctions between weak and strong coupling. *Eur. J. Phys.* **37**, 025802 (2016).
37. Ballarini, D. et al. All-optical polariton transistor. *Nat. Commun.* **4**, 1778 (2013).
38. Zasedatelev, A. et al. A room-temperature organic polariton transistor. *Nat. Commun.* **13**, 378–383 (2019).
39. Ciuti, C., Schwendimann, P. & Quattropani, A. Theory of polariton parametric interactions in semiconductor microcavities. *Semicond. Sci. Technol.* **18**, S279 (2003).
40. Ghosh, S. et al. Microcavity exciton polaritons at room temperature. *Photon. Insights* **1**, R04 (2022).
41. Gu, J. et al. Enhanced nonlinear interaction of polaritons via excitonic Rydberg states in monolayer WSe_2. *Nat. Commun.* **12**, 2269 (2021).
42. Suárez-Forero, D. G. et al. Enhancement of parametric effects in polariton waveguides induced by dipolar interactions. *Phys. Rev. Lett.* **126**, 137401 (2021).
43. Coriolano, A. et al. Rydberg polaritons in ReS_2 crystals. *Sci. Adv.* **8**, eadd8857 (2022).
44. Yoo, H., Heo, K., Ansari, M. H. R. & Cho, S. Recent advances in electrical doping of 2D semiconductor materials: methods, analyses and applications. *Nanomaterials* **11**, 832 (2021).

Methods

Sample fabrication

The DBR is formed by eight pairs of SiO_2/TiO_2 layers (thicknesses, 145/100 nm, respectively), deposited by electron-beam evaporation (Temescal Supersource), keeping the chamber at $10^{-5}/10^{-6}$ mbar throughout the process, with the sample at room temperature and in the absence of any oxygen gas flow (deposition rates, 1.0 Å s^{-1} for SiO_2 and 0.5 Å s^{-1} for TiO_2). The DBR is deposited on top of a 170 µm glass substrate and the resulting stop band is centred at 1,476 meV (840 nm).

Single-layer WS_2 is mechanically exfoliated from bulk crystals with Nitto SPV 224 tape and transferred onto the surface of a polydimethylsiloxane stamp (Gelfilm from Gel-Pak). Single-layer WS_2 is transferred by all-dry deterministic transfer procedure[45] on the DBR substrate by using a polydimethylsiloxane stamp. The sample is annealed in a vacuum at 200 °C for 2 h. Synthetic bulk WS_2 crystals were purchased from HQ Graphene.

A 20 nm SiO_2 film is deposited via electron-beam evaporation on top of the WS_2 monolayer, again in the absence of any oxygen flow and keeping the sample at room temperature. The glass surface is then spin coated with PMMA 950k at high accelerations and then degassed in a high vacuum before soft baking. After removal from the vacuum chamber, the sample is immediately soft baked, spin coated again with a thin surfactant-enhanced discharge layer and placed in the electron-beam-lithography vacuum chamber without any other baking step. The pattern is exposed to a 30 kV electron beam, using a positive-tone process at low doses; the sample is finally developed with a low-stress and low-dose developer, followed by rinsing with surfactant-enhanced deionized water and N_2 drying.

Optical measurements

All the measurements reported here are performed under ambient conditions at room temperature. The reflectivity measurements beyond the light cone are performed using a home-built microscope, equipped with a 1.42-numerical-aperture oil-immersion objective. Four lenses (Thorlabs, focal lengths of 20/30/50 cm) are used to project a magnified image of the back focal plane onto the slit of an imaging spectrometer with a cooled charge-coupled device camera. For PL measurements, the WS_2 monolayer is off-resonant excited by using a continuous-wave 488 nm diode laser. The PL is recorded in the reflection configuration, using a ×40 objective with a 0.95 numerical aperture.

For nonlinear measurements, a tunable femtosecond laser (pulse width, ~145 fs; repetition rate, 10 kHz) is focused onto the back focal plane of the 0.95-numerical-aperture objective. The energy of the laser resonantly pumping the interested polariton mode and the corresponding real-space spot-size dimensions are ~1,890 eV and ~10 μm^2, respectively.

Simulations and fits

All the electromagnetic simulations for optimizing the stack and grating geometry rely on a commercial implementation (Ansys Lumerical) of the finite-difference time-domain method, run on a 5 nm space grid and a time grid determined accordingly, based on the Courant condition for stability[46]. The actual optimization code is an in-house implementation of a particle swarm optimization algorithm[47,48]. Simulations of reflectivity are instead performed by an open-source implementation of the rigorous coupled-wave analysis method[49], using a Fourier basis of dimension 30. The experimental data reported in Fig. 2 are fitted with a 2 × 2 coupled harmonic oscillator Hamiltonian:

$$H_{\mathbf{k}} = \begin{pmatrix} E_{\mathrm{ph}}(k) & \Omega/2 \\ \Omega/2 & E_{\mathrm{exc}} \end{pmatrix}, \quad (2)$$

where E_{exc} is the exciton energy, Ω is the Rabi splitting and $E_{\mathrm{ph}}(k)$ is the energy dispersion of the BIC-like photonic branch, experimentally extrapolated from a PhC area without the TMD. We provide more details on the procedure in Supplementary Section E.

Data availability

The data that support the findings of this study are available from the corresponding authors upon reasonable request.

Code availability

The codes used in this work are available from the corresponding authors upon request.

References

45. Castellanos-Gomez, A. et al. Deterministic transfer of two-dimensional materials by all-dry viscoelastic stamping. *2D Mater.* **1**, 011002 (2014).
46. Taflove, A. & Hagness, S. C. *Computational Electrodynamics: The Finite-Difference Time-Domain Method* 3rd edn (Artech House, 2005).
47. Lindfield, G. & Penny, J. in *Introduction to Nature-Inspired Optimization* Ch. 3 (Academic Press, 2017).
48. Xu, G. & Yu, G. On convergence analysis of particle swarm optimization algorithm. *J. Comput. Appl. Math.* **333**, 65–73 (2018).
49. Liu, V. & Fan, S. S^4: a free electromagnetic solver for layered periodic structures. *Comput. Phys. Commun.* **183**, 2233–2244 (2012).

Acknowledgements

We are grateful to C. Anton-Solanas for the fruitful discussions and for the help in the optimization of the fabrication process. We gratefully thank P. Cazzato for technical support, L. Dominici for fruitful discussions on the design solutions and L. Carbone for precious support in the development of the fabrication process. We acknowledge the CINECA award under the ISCRA C initiative (D.G. and E.M.) for the availability of high-performance computing resources and support. This work was supported by the Italian Ministry of University (MIUR) for funding through the PRIN project 'Interacting photons in polariton circuits'—INPhoPOL (grant 2017P9FJBS) (D.S. and D.G.); the project 'Hardware implementation of a polariton neural network for neuromorphic computing'—Joint Bilateral Agreement CNR-RFBR (Russian Foundation for Basic Research)—Triennal Program 2021–2023 (D.S.); the MIUR project 'ECOTEC—eco-sustainable and intelligent fibers and fabrics for technic clothing', PON R&I 2014-2020, project no. ARS0100951, CUP B66C18000300005 (V.M.); the Italian Ministry of Research (MUR) under the complementary actions to the NRRP (PNC0000007) 'Fit4MedRob—Fit for Medical Robotics' (grant-contract number CUP B53C22006960001) (V.M.); the MAECI project 'Novel photonic platform for neuromorphic computing', Joint Bilateral Project Italia–Polonia, 2022–2023 (D.S.); the PNRR MUR project 'National Quantum Science and Technology Institute' (NQSTI) (D.S. and D.G.); the PNRR MUR project: European Union—NextGeneration EU, 'Integrated infrastructure initiative in photonic and quantum sciences'—I-PHOQS IR0000016, ID D2B8D520, CUP B53C22001750006 (D.S.); and the project 'TECNOMED—Tecnopolo di Nanotecnologia e Fotonica per la Medicina di Precisione' (MIUR Decreto Direttoriale no. 3449 del 4/12/2017, CUP B83B17000010001) (G.G.).

Author contributions

E.M., L.P., F.T. and A.D.R. realized the samples. E.M. and D.B. conceived the idea. E.M. developed the nanofabrication process, numerical tools and theory/data analysis. L.P. performed the optical measurements. E.M., L.P., D.B., D.G. and D.S. wrote the text. A.C., M.P. and V.M. grew the dielectric mirrors. B.H. and C.S. contributed the exfoliated TMDs and mirrors for preliminary fabrication tests. L.D.M., R.M. and A.R contributed to the preparation of the samples. D.B., D.S. and D.G. supervised the project.

All authors contributed to the discussion of the results and the text.

Competing interests
The authors declare no competing interests.

Additional information
Supplementary information The online version contains supplementary material available at https://doi.org/10.1038/s41563-023-01562-9.

Correspondence and requests for materials should be addressed to Daniele Sanvitto or Dario Ballarini.

Peer review information *Nature Materials* thanks Andrey Bogdanov and the other, anonymous, reviewer(s) for their contribution to the peer review of this work.